DUAL-DOPPLER VS. ENKF WIND ANALYSES OF THE 29-30 MAY 2004 GEARY, OKLAHOMA, SUPERCELL

Corey K. Potvin[1,2], Louis J. Wicker[2], Michael I. Biggerstaff[3], Daniel Betten[3], and Alan Shapiro[3,4]

[1]*Cooperative Institute for Mesoscale Meteorological Studies, University of Oklahoma, Norman, OK*
[2]*NOAA/OAR National Severe Storms Laboratory, Norman, OK*
[3]*School of Meteorology, University of Oklahoma, Norman, OK*
[4]*Center for Analysis and Prediction of Storms, University of Oklahoma, Norman, OK*

1. INTRODUCTION

Dual-Doppler mobile radar datasets enable the creation of 3-D wind retrievals and subsequent analyses (e.g., of parcel trajectories) that are critical to advancing our understanding of supercell thunderstorms. Maximizing the scientific value of these datasets requires advances to our knowledge of the expected errors for different analysis methods under different observational scenarios. Toward that end, Potvin et al. (2012b) examined errors in 3DVAR dual-Doppler wind analyses (hereafter, simply "dual-Doppler analyses", or DDAs) of a simulated supercell thunderstorm observed using storm-topping vs. shallow radar scanning strategies and optimal vs. narrow radar cross-beam angles. Using the same supercell simulation, Potvin and Wicker (2012; hereafter, PW12) examined errors in wind analyses obtained using ensemble Kalman filter (EnKF; Evensen 1994) radar data assimilation and compared them to DDA errors. Though the EnKF ideally improves wind analyses by optimally combining radar observations with short-term (for storm-scale applications, typically 2-5 min) numerical weather prediction (NWP) model forecasts, the results of PW12 suggest model errors and violations of the optimality conditions for the EnKF can produce low-level wind analyses inferior to those obtained from DDA if the radar cross-beam angles are sufficiently large. On the other hand, the study also identified several scenarios where the EnKF wind analysis may generally be superior to DDA, such as when the radar cross-beam angles are small or the wind field changes rapidly between successive volume scans. While assimilating dual- rather than single-radar observations generally improved the EnKF wind retrievals and subsequent vorticity and trajectory analyses, all the single-radar wind analyses were qualitatively accurate once enough data had been assimilated, and in many instances were commensurate with the dual-radar analyses. However, substantially larger errors occurred in vorticity stretching fields and circulation time series computed from the single-radar wind analyses. The present study continues the exploration of dual-Doppler and EnKF wind analysis errors using real storm-scale radar observations of the 29 May 2004 Geary, Oklahoma, tornadic supercell.

* Corresponding Author Address: Dr. Corey K. Potvin, 120 David L. Boren Blvd, Rm 4355, Norman, OK 73072; Email: corey.potvin@noaa.gov.

The observing system simulation experiment (OSSE) framework adopted in PW12 permitted rigorous evaluation and comparison of analysis errors. However, the realism of the errors in that study was uncertain given the artificiality of the errors input to the EnKF model and pseudo-observations. For example, observation errors were assumed to be normally distributed with known, spatiotemporally constant standard deviations; only a subset of the sources of typically large model error was simulated; and the representativeness of the model errors that were simulated was questionable. The converse tradeoff holds in the present, real-data, study: the model and observational errors pose a more realistic, and presumably greater, challenge to the EnKF, but analysis verification is limited by uncertainty in the true wind field. We have chosen to investigate the problem within both OSSE and (in the present study) real-data frameworks to draw more confident conclusions about the characteristics of storm-scale dual-Doppler and EnKF wind analysis errors. The following hypotheses from PW12 are further tested herein:

(1) Assimilating radar reflectivity factor (hereafter, "reflectivity") observations in addition to Doppler velocity observations generally degrades one-radar EnKF wind (hereafter, "1-EnKF") analyses.

(2) Two-radar EnKF wind ("2-EnKF") analyses, but not 1-EnKF analyses, are relatively insensitive to errors in the initialization sounding and (if reflectivity observations are not assimilated) microphysical parameterization (MP) scheme.

(3) Two-radar EnKF analyses generally do not substantially improve upon DDAs near the ground when radar data coverage and radar cross-beam angles are favorable.

(4) Once enough data have been assimilated, 1-EnKF wind analyses are qualitatively nearly as accurate as 2-EnKF wind analyses, but locally large wind errors occur in the 1-radar case that can substantially degrade subsequent analyses that use derivatives of the wind field (e.g., circulation time series).

The uncertainty in the true wind field fundamentally limits verification of our analyses. Fortunately, this does not hinder confirmation of hypotheses 2 and 3 (above) since they are concerned not with analysis errors, but with the magnitudes of differences between analyses obtained using different methods. Imprecise knowledge of the true wind field poses a greater challenge to the testing of hypotheses 1 and 4 since they make claims about the accuracy of 1-EnKF analyses. Despite this difficulty, useful inferences can be drawn in many cases by examining the differences between 2- and 1-EnKF analyses obtained using otherwise identical configurations. The majority of these differences can be confidently attributed to larger errors in the 1-EnKF analysis which, being less observationally constrained than the 2-EnKF analysis, is therefore more sensitive to errors in the model, forward operator, initial condition and observations, and to suboptimalities in the EnKF configuration. Thus, if substantial differences occur between corresponding (i.e., identical apart from the number of radar datasets assimilated) 1- and 2-EnKF analyses, it can be confidently assumed that errors are larger in the former. As will be shown later, similar reasoning can sometimes be used to evaluate the relative accuracy of two 1-EnKF analyses between which one aspect of the filter configuration (e.g., the MP scheme) is varied.

The rest of the paper is organized as follows. Descriptions of the supercell case and radar dataset, 3DVAR DDA technique, EnKF scheme, and methods for computing vertical vorticity fields, parcel trajectories and circulation time series are given in Section 2. In Section 3, we first examine the impact on our 2- and 1-EnKF analyses of assimilating reflectivity observations and of differences in the model initialization sounding and microphysics parameterization (MP) scheme. Upon finalizing our EnKF configuration, we compare kinematical and trajectory analyses obtained using DDA, 2- and 1-EnKF analysis. A summary follows in Section 4.

2. METHODS

2.1. Mobile radar dataset

The supercell thunderstorm analyzed in our experiments formed from a merger of several storms that initiated along a dryline over western Oklahoma during the afternoon of 29 May 2004. The supercell was unusually persistent, lasting for 12 hours and producing 18 tornadoes before decaying near the Oklahoma-Arkansas border. Additional event details can be found in Bluestein et al. (2007), Potvin et al. (2011), and Jung et al. (2012). Two Shared Mobile Atmospheric Research and Teaching (SMART; Biggerstaff et al. 2005) radars, SMART radar 1 (SR1) and SMART radar 2 (SR2), participating in the Thunderstorm Electrification Experiment (TELEX; MacGorman et al. 2008) collected coordinated volume scans of the storm for nearly 1.5 h (Fig. 1a). During this period, the radar cross-beam angle generally varied between 60° and 90° over the features of greatest interest: the main updraft, rear-flank downdraft (RFD) and storm inflow sector. During the first ~50 min of the data assimilation period (2353 UTC 29 May to 0043 UTC 30 May), the radars employed storm-topping sector scans spanning elevation angles ϕ from 0.5° to 33.5°. For the remainder of the assimilation period (0043-0113 UTC), SR1 used an even deeper volume coverage pattern (VCP) with ϕ between 0.5° and 58.9° (Fig. 1a), but at the cost of substantially increased $\Delta\phi$ between successive sweeps. The SR2 radar employed this deeper VCP between roughly 0043 UTC and 0055 UTC, then reverted to the original VCP. Volume scan periods averaged ~110 s for the original VCP and ~140 s for the deeper VCP. The radars sampled every 67 m in range and 1° in range and azimuth using half-power beamwidths of ~1.5°. Noisy, ground-clutter-contaminated and otherwise suspect data were manually removed from the dataset, and Doppler velocity values were manually dealiased. The nearly optimal storm-relative positioning of the radars (e.g., very favorable cross-beam angles) as well as the long duration of the dual-Doppler observational period (due largely to the relatively slow storm motion) make this one of the most scientifically useful storm-scale mobile radar datasets to date.

The supercell thunderstorm analyzed in our experiments formed from a merger of several storms that initiated along a dryline over western Oklahoma during the afternoon of 29 May 2004. The supercell was unusually persistent, lasting for 12 hours and producing 18 tornadoes before decaying near the Oklahoma-Arkansas border. Additional event details can be found in Bluestein et al. (2007), Potvin et al. (2011), and Jung et al. (2012). Two Shared Mobile Atmospheric Research and Teaching (SMART; Biggerstaff et al. 2005) radars, SMART radar 1 (SR1) and SMART radar 2 (SR2), participating in the Thunderstorm Electrification Experiment (TELEX; MacGorman et al. 2008) collected coordinated volume scans of the storm for nearly 1.5 h (Fig. 1a). During this period, the radar cross-beam angle generally varied between 60° and 90° over the features of greatest interest: the main updraft, rear-flank downdraft (RFD) and storm inflow sector. During the first ~50 min of the data assimilation period (2353 UTC 29 May to 0043 UTC 30 May), the radars employed storm-topping sector scans spanning elevation angles ϕ from 0.5° to 33.5°. For the remainder of the assimilation period (0043-0113 UTC), SR1 used an even deeper volume coverage pattern (VCP) with ϕ between 0.5° and 58.9° (Fig. 1a), but at the cost of substantially increased $\Delta\phi$ between successive sweeps. The SR2 radar employed this deeper VCP between roughly 0043 UTC and 0055 UTC, then reverted to the original VCP. Volume scan periods averaged ~110 s for the original VCP and ~140 s for the deeper VCP. The radars sampled every 67 m in range and 1° in range and azimuth using half-power beamwidths of ~1.5°. Noisy, ground-clutter-contaminated and otherwise suspect data were manually removed from the dataset, and Doppler velocity values were manually dealiased. The nearly optimal storm-relative positioning of the radars (e.g., very favorable cross-beam angles) as well as the long duration of the dual-Doppler observational period (due largely to the relatively slow storm motion) make this one of the most scientifically useful storm-scale mobile radar datasets to date.

2.2. EnKF configuration

EnKF analyses are obtained using the National Severe Storms Laboratory Collaborative Model for Multiscale Atmospheric Simulation (NCOMMAS; Wicker and Skamarock 2002; Coniglio et al. 2006) ensemble square root filter (Whitaker and Hamill 2002). Forty ensemble members are used in all the experiments presented below; repeating the 2-LFO, 1-ZVD and 2-ZVD experiments (the experiment nomenclature is described near the end of this subsection) with 80 members produced only minor differences (not shown) in the wind retrievals and subsequent kinematical analyses (Section 2f). The EnKF domain (Fig. 1b) has horizontal (vertical) dimensions of 160 km $\times$ 80 km (20 km) and horizontal (vertical) grid spacings of 1.0 km (0.5 km). Large and small time steps of 2 s and 1/3 s, respectively, were used for the model integration. The covariance localization factor is calculated using the Gaspari and Cohn (1999) correlation function with covariance estimation cutoff radii of 6 km (horizontal) and 3 km (vertical). In most experiments, the ensemble members are initialized using a sounding collected at Minco, OK at 0006 UTC 30 May (Fig. 2a). In one set of experiments, the impact of initializing the ensemble using a different sounding, collected at Weatherford, OK at 2236 UTC 29 May (Fig. 2b), is examined. To initiate storms within the ensemble, ellipsoidal thermal bubbles having random locations, dimensions and magnitudes are inserted in each member within a 40 km $\times$ 40 km box centered near the location of the supercell at 2323 UTC. The ensemble members are then integrated 30 min forward to the beginning of the data assimilation period (2353 UTC). This allows physically realistic covariances to develop in the ensemble, thus maximizing the utility of radar data early in the assimilation period (e.g., Snyder and Zhang 2003; Dowell et al. 2004). All non-UTC times (e.g., t = 60 min) in this paper are relative to the beginning of the 30 min integration (2323 UTC).

Doppler velocity observations, V^{obs}, and, in one set of experiments, reflectivity observations > 0 dBZ, Z^{obs}, are assimilated. In all experiments, to suppress spurious convection in the ensemble, reflectivity observations that are missing or < 0 dBZ, Z^{low}, are set to 0 dBZ and assimilated (i.e., used as "no-precipitation" observations; Tong and Xue 2005; Aksoy et al. 2009). Prior to assimilation, observations are analyzed to a quasi-horizontal grid on each conical scan surface (e.g., Dowell et al. 2004; Dowell and Wicker 2009) using quasi-horizontal Cressman interpolation with the cutoff radius set to half the grid spacing. Following PW12, the grid spacing is set to 2 km in the dual-radar experiments and to 1 km in the single-radar experiments. Repeating one of the dual-radar (single-radar) experiments using 1 km (1.5 km) grid spacing produced similar results, which supports the appropriateness of the chosen grid spacings. After being interpolated, observations are advection-corrected to account for storm motion between the observation and analysis times. The estimated storm translational velocity components U and V (= 12.5 m s^{-1} and 0 m s^{-1}, respectively) are treated as constants in space and time and were estimated from the displacement of the hook echo reflectivity signature between the beginning and end of the data assimilation period. Observations are assimilated every two minutes using a centered two-minute window.

As in many EnKF radar data assimilation studies, to reduce computational cost, the observation operator trilinearly interpolates model fields to observational locations, making no provision for the shape of the radar beam (several studies have included power-gain weighting in the vertical dimension, e.g., Xue et al. 2006; Jung et al. 2008; Tong and Xue 2008) nor the inhomogeneous reflectivity distribution within the beam. Thompson et al. (2012) show these simplifications do not significantly degrade the EnKF analyses. The DDA technique uses Cressman, not trilinear, interpolation to compute u, v and w at observational locations. However, we do not expect this to be a major source of the differences between the DDAs and EnKF wind analyses. The Z^{obs} operator (which is the same as the Z^{low} operator) is consistent with the microphysical parameterization scheme used in each experiment; that is, both adopt the same hydrometeor categories and particle size distribution assumptions. The V^{obs} operator and DDA technique use the same formula to estimate hydrometeor fall speeds: $w_t = -2.6Z^{.107}\left(1.2/\rho_{sim}\right)^{0.4}$, where ρ_{sim} (kg m^{-3}) is the height-varying base state air density in the simulation and Z is given in mm^6 mm^{-3} (Joss and Waldvogel 1970).

Following Dowell and Wicker (2009), to save computational time, observations are not used to update the Exner function π and turbulent mixing coefficient K_m since the impact of the observations on these variables is negligible. All three observation types are used to update the remaining NCOMMAS prognostic variables: the wind components u, v and w, potential temperature θ, water vapor mixing ratio q_v, and the microphysical state variables predicted by the MP scheme. The Z^{obs}, Z^{low} and V^{obs} error variances are set to 25 dBZ^2, 25 dBZ^2 and 9 m^{2}s^{-2}, respectively, in the filter. Radar data are assimilated for an 80 min period, during which the supercell travels eastward from northwest of SR2 to northeast of SR1 (Fig. 1b). Due to the lack of dual-radar data between roughly 0000 UTC and 0010 UTC, we begin examining dual-Doppler and EnKF wind analyses at 0011 UTC.

Two procedures are used to produce ensemble spread consistent with the ensemble forecast error variance. To account for uncertainty in the sounding, perturbations are added to the base-state u and v of each ensemble member. The perturbations are computed by generating random sinusoidal perturbations of the form used in Aksoy et al. (2009), then scaling them such that their standard deviation at each level is a fraction a of the base-state wind speed multiplied by exp(z/22), where z is the model level height in kilometers. Larger perturbations were required in the 1-EnKF experiments (a = 0.15) than in the 2-EnKF experiments (a = 0.10) to achieve desirable ensemble spread. This is presumably because twice as many observations were assimilated in the 1-EnKF experiments (while the number of assimilated radars was halved, the 2-D grid density increased by a factor of four); assimilating very dense observations can create suboptimal ensemble spread due to sampling errors arising from the finite ensemble size. Scaling the base-state *u* and *v* perturbations to the altitude and base-state winds substantially mitigated ensemble underdispersion over the top half of the domain.

The second procedure used to maintain suitable ensemble spread is similar to the additive noise method (Dowell and Wicker 2009; based on the ensemble initialization procedure of Caya et al. 2005). Smoothed perturbations having horizontal and vertical length scales of 4 km and 2 km, respectively, are added to *u*, *v*, θ, and dewpoint temperature T_d below z = 10 km wherever Z^{obs} > 20 dBZ throughout the data assimilation period. Prior to being smoothed, the *u*, *v*, θ and T_d perturbations have standard deviations of 2 m s^{-1}, 2 m s^{-1}, 1 K and 1 K, respectively (unless stated otherwise). Diagnostic statistics computed within the observation space suggest the EnKF is reasonably well configured in our experiments. For example, time-height plots of the V^{obs} consistency ratio (e.g., Dowell et al. 2004) indicate nearly optimal ensemble spread (values near unity) is achieved over the lower 10 km of the domain throughout the assimilation period in all our EnKF analyses (e.g., Figs. 3a, b). In addition, mean prior V^{obs} innovations are generally near zero (e.g., Figs. 3c, d), indicating model forecasts of the radial wind component are relatively unbiased.

Several factors are varied in the EnKF experiments. Data are assimilated either from SR2 alone (indicated in the experiment label by the prefix "1-") or from both radars (indicated by "2-"). We chose to assimilate SR2 data in the single-radar experiments because there were fewer gaps in its observational period than in that of SR1. Assimilating SR1 data instead (experiment not shown) had the expected effect: wind analyses later in the assimilation period, when the storm was closer to SR1, appeared to improve relative to when SR2 data were assimilated, while wind analyses earlier in the data assimilation period, when the storm was closer to SR2, appeared to worsen. Microphysical processes are parameterized using either the Gilmore et al. (2004) version of the Lin et al. (1983) scheme (hereafter, "LFO") or a two-moment version of the Ziegler Variable Density scheme (ZVD; Ziegler 1985; Mansell et al. 2010). As mentioned above, Z^{obs} are assimilated in addition to Z^{low} and V^{obs} in one set of experiments (denoted by "-Z"), and in another set of experiments (denoted by "-W"), the Weatherford, Oklahoma sounding is used rather than the Minco, OK sounding (Fig. 2) to initialize the ensemble.

2.3. 3DVAR DDA technique

The 3D-VAR dual-Doppler analyses are obtained using the technique described in Shapiro et al. (2009) and Potvin et al. (2012a). The technique weakly satisfies the radial wind observations, the anelastic mass conservation equation and a smoothness constraint, and exactly satisfies the impermeability condition at the ground (since low-level data were available in our experiments there was no need to invoke the vorticity equation constraint tested in the aforementioned studies). Provision is made for wind field translation between the analysis and observational times using the same space-time transformation as in the EnKF experiments except that the *u*, *v* and *w* fields are shifted to each observation location prior to computing the analyzed radial winds. Potvin et al. (2012c) demonstrated that the advantages afforded by the 3DVAR framework (Gao et al. 1999) may produce better storm-scale wind retrievals than traditional DDA methods near the ground and toward the top of the storm.

The DDAs are valid at the beginning of each coordinated volume scan within the data assimilation period (Table 1). The interval between successive DDAs is generally ~2.5-3.5 min. The analyses proceed on a 40 × 40 × 20 km domain (Fig. 1b) with horizontal and vertical grid spacings of 1.0 and 0.5 km, respectively (as in the EnKF grid). The DDA grid is periodically recentered on the storm to avoid truncating the important portion of the wind field.

2.4. Computing vorticity, parcel trajectories and circulation

In all experiments, the vertical vorticity, $\zeta \equiv \partial v/\partial x - \partial u/\partial y$, is computed from the analyzed wind field. The use of an unstaggered (Arakawa-A) grid for the DDAs and an Arakawa-C grid for the EnKF analyses precludes using the same stencil to compute ζ on both analysis grids. We decided to compute ζ using centered finite differences valid over 2Δ in both cases, requiring that the EnKF *u* and *v* be meridionally and zonally interpolated, respectively, to the DDA grid prior to computing ζ.

In several experiments, the fourth-order Runge-Kutta method is used to backward-compute parcel trajectories from series of DDAs (available every ~5.5 min in one set of experiments and every ~3 min in the other) and EnKF wind analyses (available every 2 min). The trajectory time step is 1 s. Linear temporal interpolation is used to estimate the wind field at times intermediate to the DDA and EnKF analysis times. Material circuits *C* connecting the parcel trajectories at successive times are computed. Finally, time series of circulation, $\Gamma \equiv \sum_{C} \mathbf{V} \bullet d\mathbf{l}$, where $d\mathbf{l}$ is the line element vector tangent to *C* at a given point, are computed around the material circuits.

2.5. Comparing 1-EnKF analyses

As stated in the introduction, in cases where substantial differences occur between a 1-EnKF analysis and its corresponding (i.e., identical apart from the number of radar datasets assimilated) 2-EnKF analysis, a large portion of those differences presumably arises from errors in the less observationally constrained 1-EnKF analysis.

Fortunately, similar reasoning can be used in some cases to identify the better of two 1-EnKF analyses between which one aspect of the filter configuration (e.g., the microphysics parameterization scheme) is varied. For example, in the event that one 1-EnKF analysis is substantially more similar than another 1-EnKF analysis to both of their corresponding 2-EnKF analyses, the former 1-EnKF analysis can be confidently supposed to be superior to the latter 1-EnKF analysis. To see why this is true, and why making such a determination requires that one of the 1-EnKF analyses provides a better match than the other to *both* 2-EnKF analyses, consider a pair of 1-EnKF analyses obtained using identical procedures except one employs method A (1-A) and the other method B (1-B). Suppose it is initially unknown which of their corresponding 2-EnKF analyses, 2-A and 2-B, is superior, but that both analyses can be safely assumed to be superior to both 1-A and 1-B (since they assimilate data from two radars rather than one). Now, if 1-A provides a better match than 1-B to 2-A, but 1-B provides a better match than 1-A to 2-B, then it is plausible that 1-A better matches 2-A primarily because much of the error arising from A is common to 1-A and 2-A (since both use method A), and that 1-A and 2-A are actually inferior to 1-B and 2-B, respectively (of course, it is just as plausible that 1-B and 2-B are inferior to 1-A and 2-A, respectively). If, on the other hand, 1-A also provides a better match than 1-B to 2-B *despite* the inherent commonalities (by virtue of B) between the latter two analyses, the only plausible explanation is that B produces larger errors than A, since if this was not the case, it would be highly improbable that 1-A provides a better match than 1-B to 2-B. Of course, in the scenario where 1-A and 1-B are very similar to each other, it can be concluded that neither A nor B introduces substantially larger errors than the other.

2.6. Verification

The verification procedure is designed to de-emphasize small-scale differences between the various wind retrievals. This is because the reliability of the 2-radar analyses (which, again, are used as a proxy for "truth") is more questionable at scales approaching the minimum resolvable wavelength (twice the grid spacing, i.e., 2 km in our experiments). We chose to evaluate and compare the wind retrievals primarily using time-height plots of mean $w > 20$ m s^{-1} (i.e., the mean of all w that exceed 20 m s^{-1} at a given height and time) and mean $\zeta > 0.01$ s^{-1}; time-height plots of correlation coefficients and RMS differences between (non-thresholded) w analyses; and horizontal cross-sections of the w, ζ and storm-relative horizontal winds at $z = 0.5$ km. Hereafter, all these analyses are referred to collectively as the "kinematical analyses". All of the kinematical analyses are valid over the set of DDA domain (Fig. 1b) gridpoints laying within 1.5 km of at least one V^{obs} (on the spherical radar grid) from each radar.

3. RESULTS

3.1. Impact of Z^{obs} assimilation

In our first set of experiments, we examined the impact of assimilating Z^{obs} on the EnKF wind analyses. In the 2-radar experiments, Z^{obs} and Z^{low} were only assimilated from one radar (SR2) since the reflectivity observations from the other radar would have provided little independent information. In the 1-radar experiments, the amplitudes of the additive noise perturbations were multiplied by four to obtain suitable ensemble spread (consistency ratios). The overall value to the wind analyses of assimilating Z^{obs} was similar whether the ZVD or the LFO MP scheme was used; only results from the LFO experiments are discussed below.

Assimilating Z^{obs} substantially affected the 1-EnKF analyses, and had much less impact on the 2-EnKF analyses (Figs. 4a, 4b, 5). In both cases, the largest differences occurred early in the evaluation period, during which comparisons of the observed and EnKF-analyzed Z as well as of the dual-Doppler- and EnKF-analyzed winds (not shown) indicated the ensemble covariances were still improving as more observations were assimilated (i.e., ensemble "spin-up" was still in progress). For example, the mean $w > 20$ m s^{-1} prior to $t = 55$ min were generally much weaker when the Z^{obs} were assimilated, especially in the 1-radar case (Fig. 5, right column).

Time-height correlations between the w obtained in the single- and dual-radar experiments (Figs. 4c-f, top panels) indicate that, at low levels during the $t = 58$ - 68 min period, the 1-LFO w diverges more than the 1-LFO-Z w from the 2-LFO w and 2-LFO-Z w. Following the reasoning of Section 3e, we infer that the majority of these differences comprise errors in the 1-LFO analysis. After $t = 68$ min, the 1-LFO w appear mildly better than the 1-LFO-Z w at low levels. In many instances, however, neither low-level analysis is definitively better than the other. A representative example of this is shown in Fig. 5 (left column). While the low-level circulation appears to be better represented in the 1-LFO-Z analysis than in the 1-LFO analysis, the magnitude of the local downdraft extremum just southeast of the vorticity maximum appears better captured in the 1-LFO analysis. In addition, the horizontal winds near $x = -40$ km, $y = 35$ km appear much better analyzed in the 1-LFO analysis than in the 1-LFO-Z analysis. In this and many other instances where large errors occur in the 1-LFO-Z u and v, the true horizontal flow (approximated by the 2-LFO and 2-LFO-Z analyses) is largely perpendicular to the radar beam. This result is consistent with the expectation that errors from the MP scheme, forward operator and other sources will degrade the wind analysis more when the 3-D wind field is less constrained by the V^{obs}.

At middle and upper levels, both the correlation and RMS difference plots suggest the 1-LFO w is generally superior to the 1-LFO-Z w (cf. Figs. 4c,d; cf. Figs. 4e,f). This conclusion is further supported by comparisons of the mean $w > 20$ m s^{-1} plots, which reveal a general lack of intense updraft in the 1-LFO-Z analysis, punctuated by instances where too much intense updraft is present (e.g., z > 9 km around t = 75 min; Fig. 5c, right panel). Finally, mean and RMS innovations for the (unassimilated) SR1 observations (not shown) are larger for 1-LFO-Z than for 1-LFO, further confirming the larger wind errors in the former analysis. Since assimilating Z^{obs} generally degraded the wind analyses, only V^{obs} and Z^{low} were assimilated in all subsequent experiments.

The failure of reflectivity assimilation to improve EnKF wind analyses in both PW12 and in the present study is not very surprising. As discussed in Tong and Xue (2005) and Dowell et al. (2011), Z^{obs} assimilation is considerably more problematic than V^{obs} assimilation due to the typically large errors in the model-predicted reflectivity and in the reflectivity observation operator, occasionally severe measurement biases (e.g., from beam attenuation and radar miscalibration), and the nonlinear relationship between reflectivity and the model state variables. Indeed, prior RMS Z^{obs} innovations computed over the lowest 10 km of the analysis domain at each analysis time were generally 8-10 dBZ in all of our experiments (not shown), suggesting that large biases existed in the Z^{obs}, model-predicted microphysical variables and/or the Z^{obs} forward operator. The small impact of Z^{obs} assimilation in the 2-EnKF experiments after the ensemble spin-up phase suggests the dual-Doppler V^{obs} constrained the wind analysis well enough to mitigate errors from the suboptimal Z^{obs} assimilation (the same conclusion was reached in PW12).

It should be noted that no attempt was made to correct for reflectivity attenuation in our experiments. Incorporating reflectivity attenuation correction into the EnKF data assimilation procedure is a potentially effective strategy for reducing Z^{obs} bias (Xue et al. 2009). Inspection of reflectivity PPIs (not shown), however, suggests severe reflectivity attenuation in our dataset is largely confined beyond (with respect to the radars) the precipitation core (typical of C-band radar observations), and thus did not substantially impact our kinematical analyses, which are largely focused near the primary storm circulation.

3.2. Sensitivity to initialization sounding and MP scheme

In PW12, systematic errors in the low-level v in the sounding used to initialize the ensemble had little impact on the EnKF wind analyses in the 2-radar case and slightly larger impact in the 1-radar case. To explore the impact of differences in the base-state u, v, q_v and θ on our analyses, we repeated the 2-ZVD, 2-LFO, 1-ZVD and 1-LFO experiments using the Weatherford, OK sounding ("-W" experiments) rather than the Minco sounding (Fig. 2). Some potentially important differences exist between the two soundings. Most important to our purpose, substantial differences exist at many levels between the sounding winds (Fig. 2c), which could lead to substantial differences between the wind analyses in regions insufficiently constrained by the V^{obs} (particularly in the 1-radar case). In addition, some of the differences between the two soundings conceivably create systematic differences in the general storm evolution and, thus, in the EnKF forecasts (priors). For example, the interpolated (to the model vertical grid) Weatherford sounding contains no convection inhibition (CIN) below the level of free convection (LFC = 811 hPa), whereas the Minco sounding contains a small amount of CIN between its lifted condensation level (LCL) of 846 hPa and LFC of ~710 hPa. It is also noteworthy that the medium-layer storm-relative environmental helicity (SREH) is ~40 % higher in the Weatherford sounding (468 $m^2 s^{-2}$) than in the Minco sounding (334 $m^2 s^{-2}$).

As in the previous subsection, the sensitivity of the kinematical analyses to the choice of sounding was similar whether the ZVD or LFO scheme was used, and we again present results from the LFO analyses only. Consistent with the OSSEs of PW12, initializing the ensemble using the Weatherford sounding rather than the Minco sounding had very little impact on the 2-EnKF analyses, and a slightly greater, but not particularly substantial, impact on the 1-EnKF analyses (Fig. 6). As in the Z^{obs} assimilation experiments, the largest differences often occurred in regions where the flow was largely perpendicular to the radar beam. The differences between the kinematical analyses (not shown) were generally slightly smaller than those in Section 2a, and comparisons with the 2-EnKF analyses (not shown) failed to determine which (if either) sounding produced generally better results in the 1-radar case. The Minco sounding was used in all subsequent experiments.

Results of PW12 suggest that, if Z^{obs} are not assimilated, 2-radar, but not 1-radar, EnKF wind analyses are relatively insensitive to the choice of MP scheme. Consistent with that hypothesis, kinematical analyses from 2-ZVD and 2-LFO were very similar to each other (cf. Figs. 7a,b), with larger differences occuring between the 1-ZVD and 1-LFO analyses (cf. Figs. 7c,d). As examples of the latter, note the differences between the analyzed downdraft extremum west of the low-level vorticity maximum, and between the mean w > 20 m s^{-1} after t = 90 min. As in the previous two sets of experiments, it was indeterminate whether one MP scheme produced more accurate wind retrievals than the other in the 1-radar case.

3.3. Comparisons of DDAs, 1- and 2-EnKF analyses

Having finalized our EnKF configuration, we now examine the differences between dual-Doppler, 2-EnKF and 1-EnKF analyses for our case. The 2-LFO and dual-Doppler wind analyses are generally very similar at low levels within the dual-Doppler domain. In the OSSEs of PW12, which featured similarly favorable radar cross-beam angles, the 2-EnKF analyses were slightly worse than DDAs just above the ground, even when the model was perfect apart from having coarser spatial resolution than the "truth" simulation. Since it is impossible in the present study to confidently attribute differences between the DDA and 2-EnKF analyses to errors in one analysis or the other, we cannot determine whether using the EnKF generally improves, degrades, or neutrally impacts low-level wind retrievals in this case. It is useful to note, however, that the differences between the low-level winds obtained from the DDA and 2-radar EnKF analyses (column 1 of Fig. 8) are roughly as small as those obtained in PW12 (their Figs. 5 and 9). Regardless of what portions of these differences comprise increased errors or improvements in the EnKF analysis relative to the DDA, the smallness of these differences further support the PW12 hypothesis that use of EnKF radar data assimilation does not substantially improve low-level wind analyses when high-quality dual-Doppler radar data are available. The reader is reminded, however, that PW12 also found that when cross-beam angles were narrow (a common scenario due to the difficulties of mobile radar deployment), 2-radar EnKF analyses improved upon DDAs due to the greater dependence of the latter on the quality of the observational input.

As in the imperfect-model experiments of PW12, once enough data have been assimilated, the 2-EnKF and 1-EnKF wind analyses in the present study are qualitatively similar to each other, but locally substantial quantitative differences arise. For example (again making use of the assumption that the majority of the differences between the 1- and 2-radar analyses are errors in the former), we infer that the updraft along the southern portion of the gust front is underestimated in the 1-LFO analysis throughout the assimilation period (e.g., compare left panels of Fig. 8). As in previous experiments, larger 1-EnKF errors often occur in regions of largely cross-beam flow, for example, northeast of the primary circulation in Fig. 8c (left column). The locally larger errors in the 1-LFO u and v cause the low-level vorticity in the storm to be overestimated during the t = 60-70 min period, and thereafter have an overall negative, but less substantial, impact on the analysis of the evolution of intense vorticity (Fig. 8, middle column). Similarly, the mean $w > 20$ m s^{-1} in the 1-LFO analysis differs substantially from that in both 2-radar analyses (implying errors in the 1-LFO analysis) at certain heights/times (e.g., z = 2-8 km near t = 65 min; cf. right panels of Fig. 8), and appears mildly degraded overall. These results support the conclusion of PW12 that use of the EnKF formalism does not totally compensate for lack of dual-Doppler data. With respect to all three types of analysis presented in Fig. 8, however, assimilating only single-radar data does not severely degrade the results.

3.4. Parcel trajectories and circulation time series

Storm-scale wind retrievals are often used to derive analyses well-suited to illuminating important storm processes. To investigate the sensitivity of such analyses to the wind retrieval method, we now examine the differences between material circuits and circulation time series computed from the dual-Doppler, 2-LFO and 1-LFO wind analyses. One thousand parcel trajectories were backward-computed from 3-km-radius rings roughly centered on the analyzed ζ maximum at z = 1 km (low-level mesocyclone) and z = 4 km (mid-level mesocyclone) at t = 70 min and t = 96 min (0033 UTC and 0059 UTC, respectively). The majority of the trajectories in three of the four cases (the exception being the set of trajectories initialized at z = 4 km, t = 96 min) descended well below the radar data floor by t - 5 min. Since trajectory and circulation calculations prior to this time were likely contaminated by extrapolation errors in the wind retrievals in those three cases, we only evaluated the analyses between t and t – 5 min.

Horizontal projections of the material circuits connecting each set of trajectories at t – 5 min are shown in Fig. 9, and time series of the circulation computed around the circuits are shown in Fig. 10. Consistent with PW12, the DDA and 2-LFO trajectory and circulation analyses are generally qualitatively similar to each other (though larger differences occur between these analyses at t = 70 min, z = 4 km). The 1-EnKF analyses, however, differ somewhat more substantially from the 2-radar analyses than in PW12, a result that we partly attribute to the larger wind gradients associated with the much stronger resolved vortex in the present case. It is also possible that model errors are significantly larger in this real-data case than in PW12, thus increasing the degree to which the wind analyses are degraded when only single-radar data are assimilated. The 1-LFO-analyzed circulation is generally weaker than that computed from the 2-radar analyses, especially in the t = 70 min, z = 1 km case (Fig. 10a). Moreover, while the trends in the DDA- and 2-LFO-analyzed circulation are generally similar to each other, the 1-LFO-analyzed circulation evolves very differently in the z = 1 km cases (Figs. 10a, b), thereby potentially leading to severe errors in inferences about vorticity generation processes. In the t = 70 min, z = 1 km case, the 2-LFO-analyzed circulation increases by ~40 % (~1.5×10^5 m^2 s^{-2}), while the 1-LFO-analyzed circulation increases by ~700 % (~3.5×10^5 m^2 s^{-2}), thereby implying (via the Bjerknes circulation theorem) much stronger baroclinic and/or frictional vorticity generation than likely occurred during this period.

4. SUMMARY

The observing system simulation experiments of Potvin and Wicker (2012) permitted rigorous examination of storm-scale supercell wind analysis errors from DDA and 1- and 2-radar EnKF radar data assimilation. Several of the hypotheses advanced by that study were tested herein using real mobile radar observations of the 29-30 May 2004 Geary, Oklahoma supercell. The following conclusions are supported by both the simulated- and real-data experiments: (1) in the single-radar case, assimilating radar reflectivity factor observations in addition to Doppler velocity observations does not generally improve, and may degrade, EnKF wind analyses; (2) 2-radar EnKF analyses, but not 1-radar EnKF analyses, are relatively insensitive to typical errors in the initialization sounding and (if reflectivity observations are not assimilated) microphysical parameterization scheme; (3) 2-radar EnKF analyses generally do not substantially improve upon (and based on the results of Potvin and Wicker 2012, may actually degrade) DDAs near the ground when radar data coverage and cross-beam angles are favorable; and (4)

1-radar EnKF analyses are generally nearly as accurate as 2-radar EnKF analyses once enough data have been assimilated, but substantial errors can occur in localized regions of the wind field and (especially) in subsequent analyses that are vital to illuminating storm dynamics. Based on this last conclusion, *we strongly recommend continued use of dual- and multiple-Doppler radar deployment strategies in mobile field campaigns*.

Acknowledgments. The first author was supported by a National Research Council Research Associateship Award at the NOAA/National Severe Storms Laboratory.

REFERENCES

Aksoy, A., D. C. Dowell, and C. Snyder, 2009: A multicase comparative assessment of the ensemble Kalman filter for assimilation of radar observations. Part I: Storm-scale analyses. *Mon. Wea. Rev.*, **137**, 1805–1824.

Biggerstaff, M. I., and Coauthors, 2005: The Shared Mobile Atmospheric Research and Teaching Radar: A collaboration to enhance research and teaching. *Bull. Amer. Meteor. Soc.*, **86**, 1263–1274.

Bluestein, H. B., M. M. French, R. L. Tanamachi, S. Frasier, K. Hardwick, F. Junyent, and A. L. Pazmany, 2007: Close-range observations of tornadoes in supercells made with a dual-polarization, X-band, mobile Doppler radar. *Mon. Wea. Rev.*, **135**, 1522–1543.

Coniglio, M. C., D. J. Stensrud, and L. J. Wicker, 2006: Effects of upper-level shear on the structure and maintenance of strong quasi-linear mesoscale convective systems. *J. Atmos. Sci.*, **63**, 1231–1252.

Dowell, D. C., and L. J. Wicker, 2009: Additive noise for storm-scale ensemble data assimilation. *J. Atmos. Oceanic Technol.*, **26**, 911–927.

____, F. Zhang, L. J. Wicker, C. Snyder, and N. Andrew Crook, 2004: Wind and temperature retrievals in the 17 May 1981 Arcadia, Oklahoma, supercell: Ensemble Kalman filter experiments. *Mon. Wea. Rev.*, **132**, 1982–2005.

____, L. J. Wicker, and C. Snyder, 2011: Ensemble Kalman filter assimilation of radar observations of the 8 May 2003 Oklahoma City supercell: Influences of reflectivity observations on storm-scale analyses. *Mon. Wea. Rev.*, **139**, 272–294.

Evensen, G., 1994: Sequential data assimilation with a nonlinear quasi-geostrophic model using Monte-Carlo methods to forecast error statistics. *J. Geophys. Res.*, **99,** (C5). 10143–10162.

Gaspari, G., and S. E. Cohn, 1999: Construction of correlation functions in two and three dimensions. *Quart. J. Roy. Meteor. Soc.*, **125,** 723–757.

Gilmore, M. S., J. M. Straka, and E. N. Rasmussen, 2004: Precipitation uncertainty due to variations in precipitation particle parameters within a simple microphysics scheme. *Mon. Wea. Rev.*, **132,** 2610–2627.

Joss, J., and A. Waldvogel, 1970: Raindrop size distribution and Doppler velocities. Preprints, 14th Conf. on Radar Meteorology, Tucson, AZ, Amer. Meteor. Soc.

Jung, Y., M. Xue, G. Zhang, and J. M. Straka, 2008: Assimilation of simulated polarimetric radar data for a convective storm using the ensemble Kalman filter. Part I: Observation operators for reflectivity and polarimetric variables. *Mon. Wea. Rev.*, **136**, 2228–2245.

,____, ____, and M. Tong, 2012: Ensemble Kalman filter analyses of the 29-30 May 2004 Oklahoma tornadic thunderstorm using one- and two-moment bulk microphysics schemes, with verification against polarimetric radar data. *Mon. Wea. Rev.*, in press.

Lin, Y-L., R. D. Farley, and H. D. Orville, 1983: Bulk parameterization of the snow field in a cloud model. *J. Climate Appl. Meteor.*, **22,** 1065–1092.

MacGorman, D. R., W. D. Rust, T. J. Schuur, M. I. Biggerstaff, J. M. Straka, C. L. Ziegler, E, R. Mansell, E. C. Bruning, K. M. Kuhlman, N. R. Lund, N. S. Biermann, C. Payne, L. D. Carey, P. R. Krehbiel, W. Rison, K. B. Eack, and W. H. Beasley, 2008: TELEX: The Thunderstorm Electrification and Lightning Experiment, *Bull. Amer. Meteor. Soc.*, **89**, 997-1013.

Mansell, E. R., C. L. Ziegler, and E. C. Bruning, 2010: Simulated electrification of a small thunderstorm with two-moment bulk microphysics. *J. Atmos. Sci.*, **67**, 171–194.

Potvin, C. K., and L. J. Wicker, 2012: Comparison between dual-Doppler and EnKF storm-scale wind analyses: Observing system simulation experiments with a supercell thunderstorm. *Mon. Wea. Rev.*, in press.

____, A. Shapiro, M. I. Biggerstaff, and Joshua M. Wurman, 2011: The VDAC technique: A variational method for detecting and characterizing convective vortices in multiple-Doppler radar data. *Mon. Wea. Rev.*, **139**, 2593–2613.

____, C. K., A. Shapiro, and M. Xue, 2012a: Impact of a vertical vorticity constraint in variational dual-Doppler wind analysis: Tests with real and simulated supercell data. *J. Atmos. Oceanic Technol.*, **29**, 32-49.

____, L. J. Wicker, and A. Shapiro, 2012b: Assessing errors in variational dual-Doppler wind syntheses of supercell thunderstorms observed by storm-scale mobile radars. *J. Atmos. Oceanic Technol.*, **29**, 1009-1025.

____, D. Betten, L. J. Wicker, K. L. Elmore, and M. I. Biggerstaff, 2012c: 3DVAR vs. traditional dual-Doppler retrieval of a simulated supercell thunderstorm. *Mon. Wea. Rev.*, in press.

Shapiro, A., C. K. Potvin, and J. Gao, 2009: Use of a vertical vorticity equation in variational dual-Doppler wind analysis. *J. Atmos. Oceanic Technol.*, **26**, 2089–2106.

Snyder, C., and F. Zhang, 2003: Assimilation of simulated Doppler radar observations with an ensemble Kalman filter. *Mon. Wea. Rev.*, **131**, 1663–1677.

Thompson, T. E., L. J. Wicker, and X. Wang, 2012: Impact from a volumetric radar-sampling operator for radial velocity observations within EnKF supercell assimilation. *J. Atmos. Oceanic Technol*., in press.

Tong, M., and M. Xue, 2005: Ensemble Kalman filter assimilation of Doppler radar data with a compressible nonhydrostatic model: OSS Experiments. *Mon. Wea. Rev.*, **133**, 1789–1807.

____, and ____, 2008: Simultaneous estimation of microphysical parameters and atmospheric state with radar data and ensemble Kalman filter. Part I: Sensitivity analysis and parameter identifiability. *Mon. Wea. Rev.*, **136,** 1630–1648.

Whitaker, J. S., and T. M. Hamill, 2002: Ensemble data assimilation without perturbed observations. *Mon. Wea. Rev.*, **130**, 1913–1924.

Wicker, L. J., and W. C. Skamarock, 2002: Time-splitting methods for elastic models using forward time schemes. *Mon. Wea. Rev.*, **130**, 2088–2097.

Xue, M., M. Tong, and K. K. Droegemeier, 2006: An OSSE framework based on the ensemble square root Kalman filter for evaluating the impact of data from radar networks on thunderstorm analysis and forecasting. *J. Atmos. Oceanic Technol.*, **23**, 46–66.

____, ____, and G. Zhang, 2009: Simultaneous state estimation and attenuation correction for thunderstorms with radar data using an ensemble Kalman filter: tests with simulated data. *Quart J. Roy. Meteor. Soc*., **135**, 1409–1423.

Ziegler, C. L., 1985: Retrieval of thermal and microphysical variables in observed convective storms. Part 1: Model development and preliminary testing. *J. Atmos. Sci.*, **42**, 1487–1509.

DDA Analysis No.	Valid times (UTC)
1	001109
2	001355
3	001641
4	001925
5	002210
6	002741
7	003311
8	003622
9	003841
10	004225
11	004545
12	004857
13	005213
14	005527
15	005843
16	010158
17	010512
18	010828
19	011142

Table 1. DDA times (UTC) in HHMMSS format.

(a)

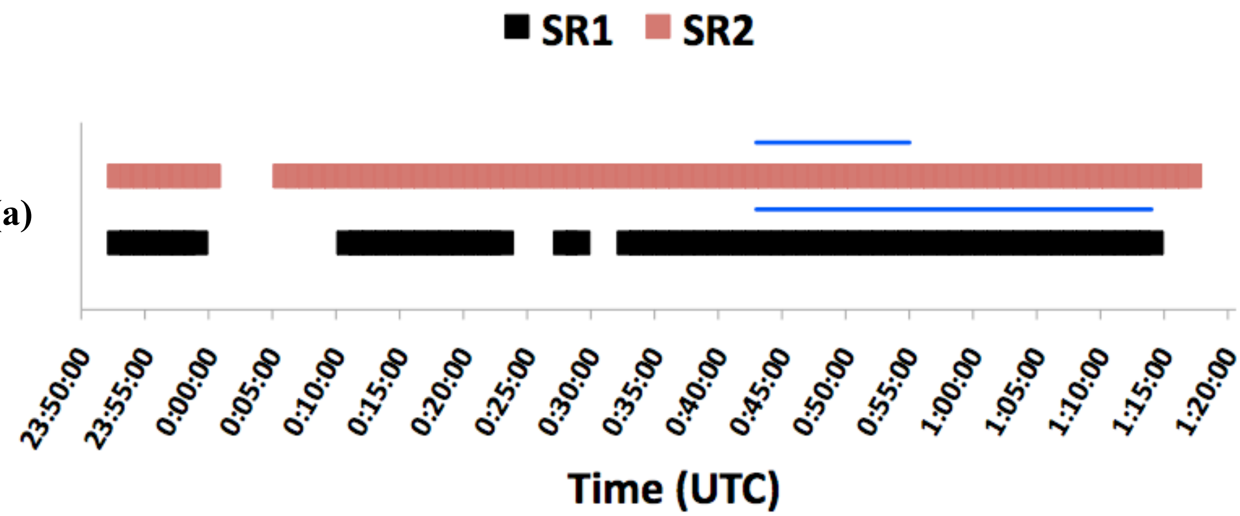

(b)

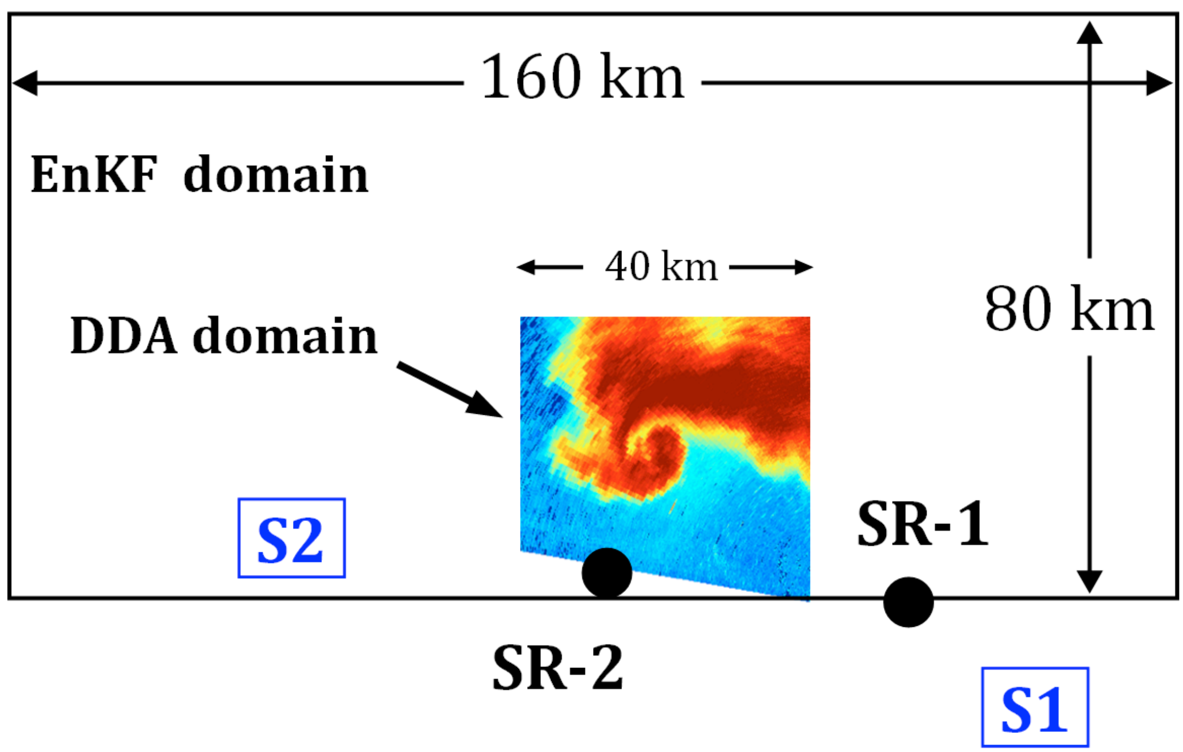

Figure 1. (a) Temporal coverage of radar data during assimilation period. The blue lines indicate periods during which each radar used the deeper, vertically coarser VCP. (b) Spatial data assimilation domain, SR1 and SR2 locations, and SR1 Z^{obs} within DDA/evaluation domain at 0033 UTC. The release location of the sounding used to initialize the ensemble member base states in most experiments (in Section 3b experiments) is denoted by "S1" ("S2").

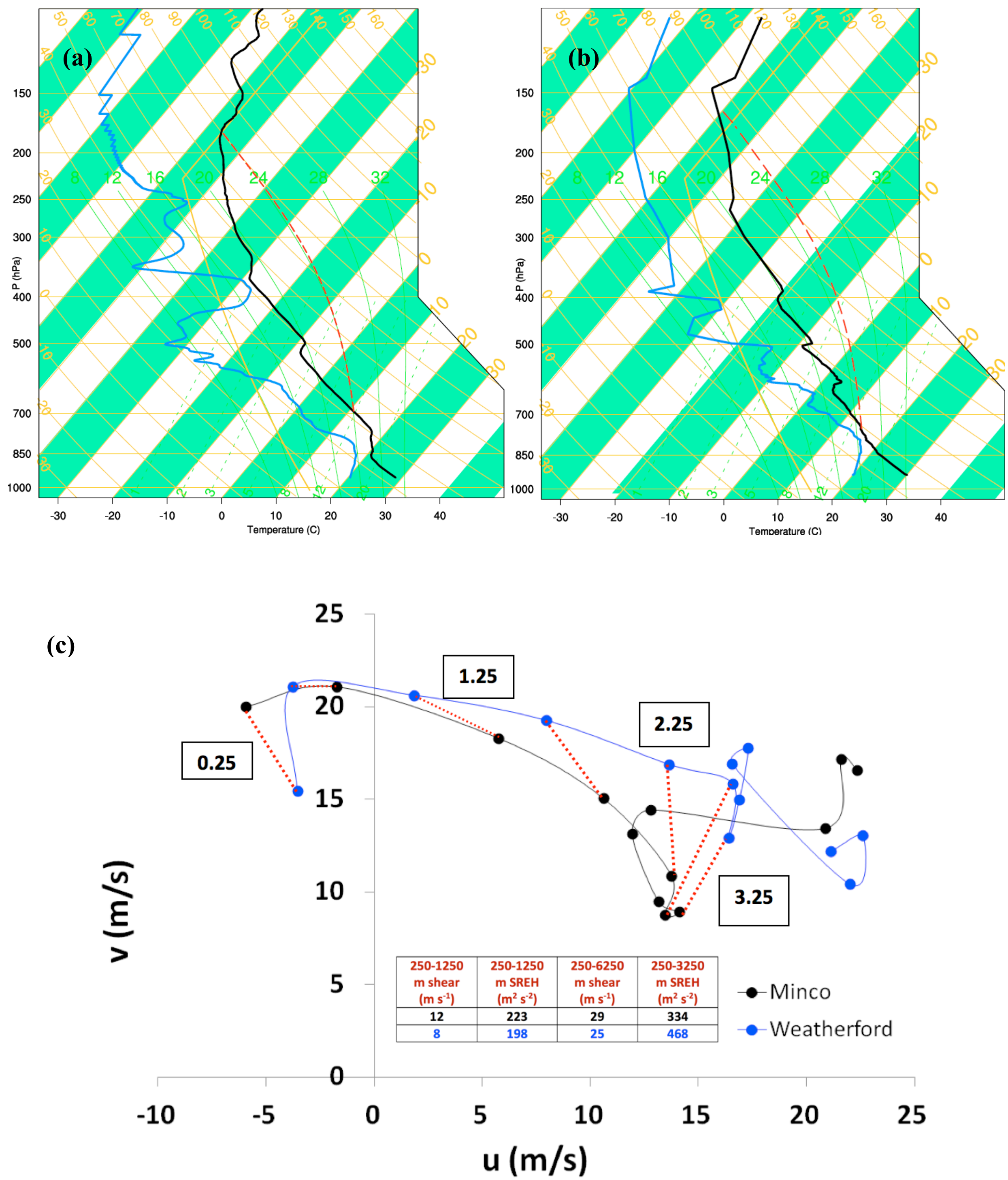

Figure 2. (a) Interpolated (to model vertical grid) Minco sounding used to initialize ensemble in most experiments. (b) Interpolated Weatherford sounding used to initialize ensemble in Section 3b experiments. (c) Hodographs (z = 250 m to 6250 m) from the two soundings (Minco = black, Weatherford = blue). Bulk wind shear and SREH values for each sounding are listed in the embedded table. Red dashed lines connect the hodographs every 0.5 km in height.

(a) **(b)**

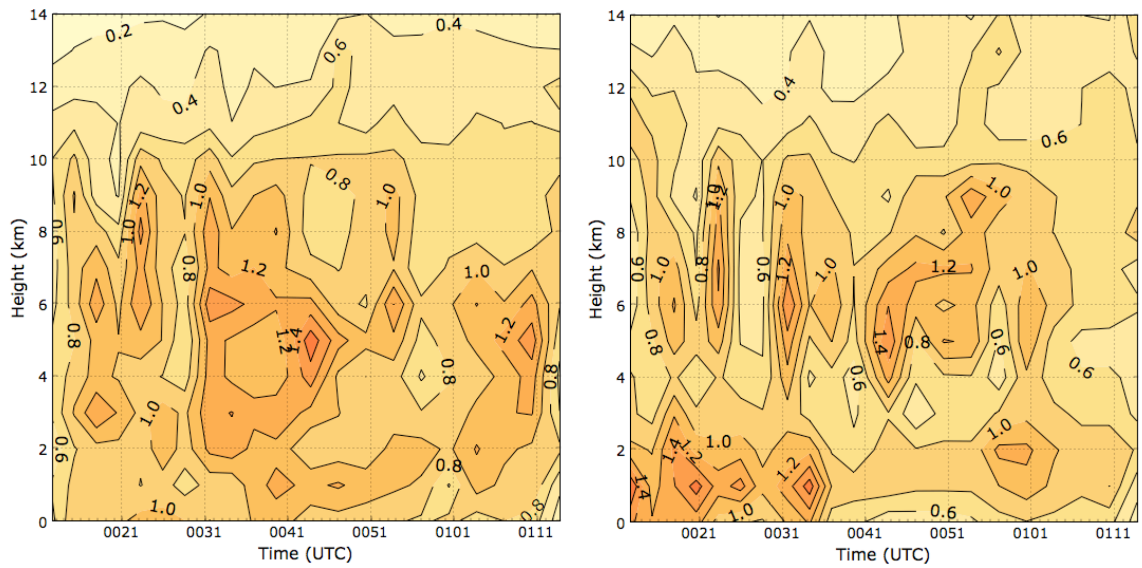

(c) **(d)**

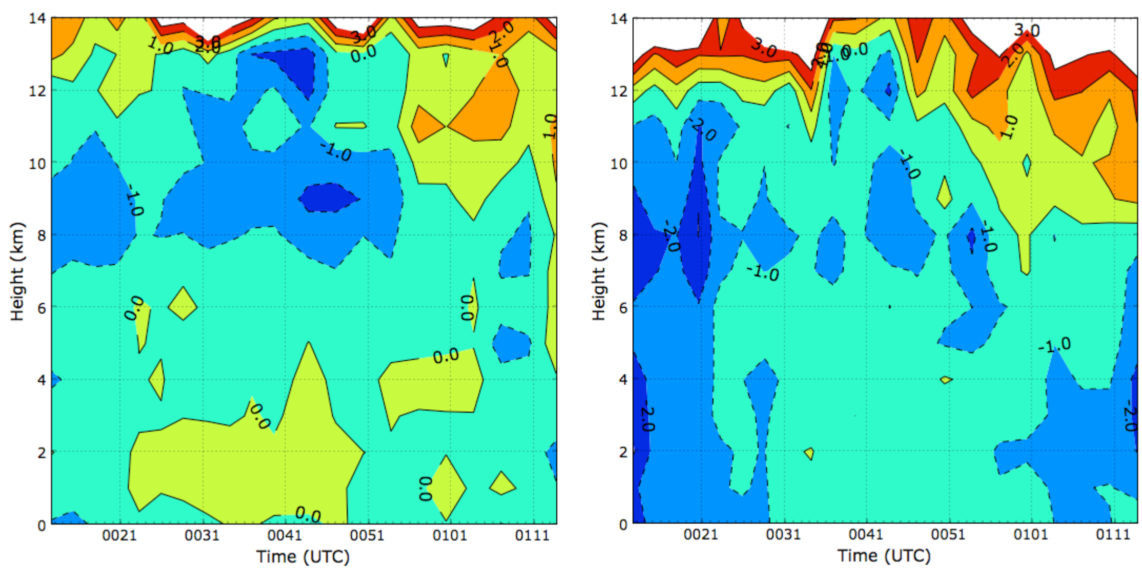

Figure 3. Time-height plots of consistency ratio (top panels) and mean forecast innovation (bottom panels) for V^{obs} (for Z^{obs} > 10 dBZ) in 2-LFO (left panels) and 1-LFO (right panels) analyses. Statistics were computed every 1 km in height over 4-min intervals roughly centered on the middle time of each volume scan.

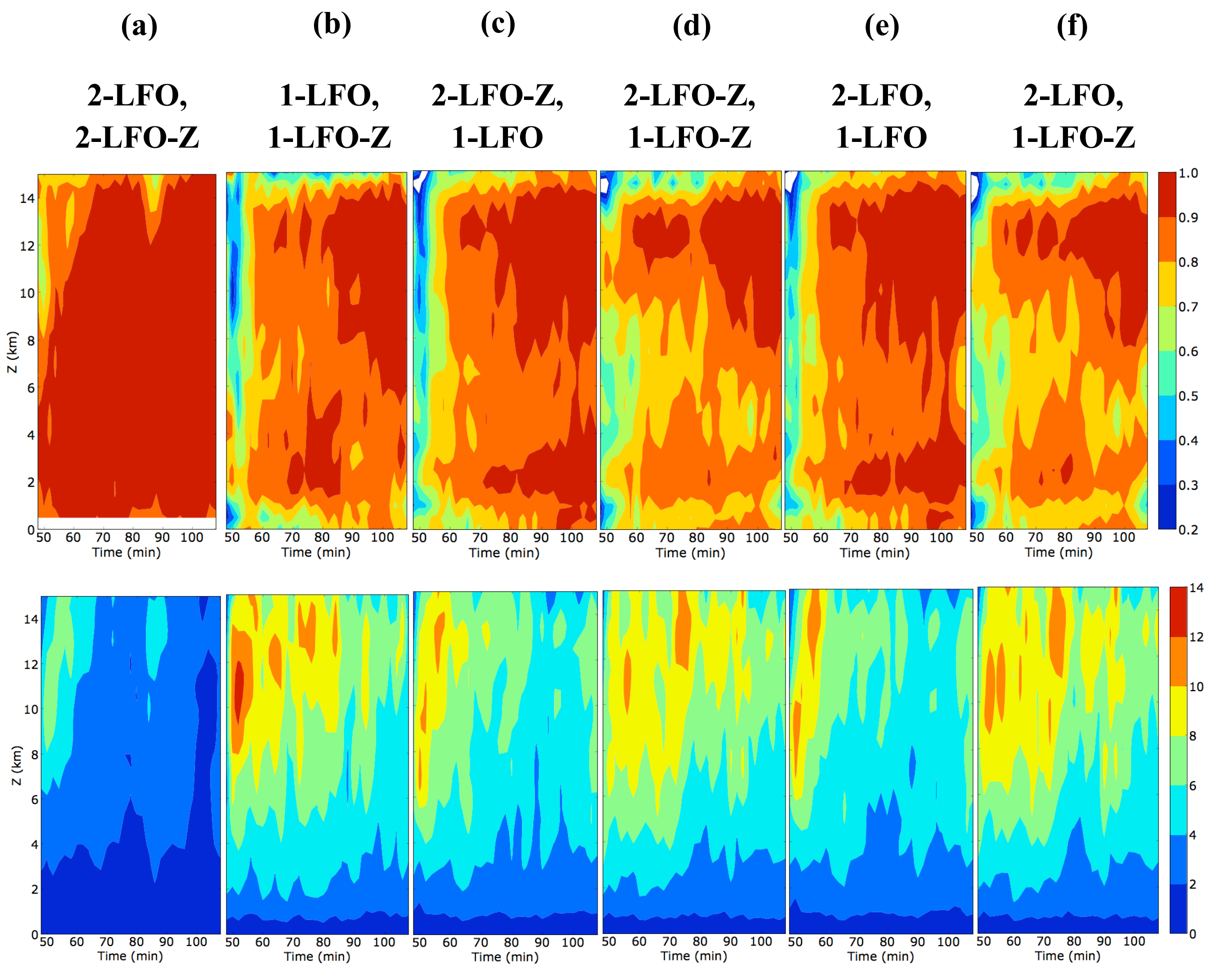

Figure 4. Time-height plots of (top) correlation coefficient and (bottom) RMS difference between *w* from (a) 2-LFO and 2-LFO-Z, (b) 1-LFO and 1-LFO-Z, (c) 2-LFO-Z and 1-LFO, (d) 2-LFO-Z and 1-LFO-Z, (e) 2-LFO and 1-LFO, (f) 2-LFO and 1-LFO-Z. In this and subsequent figures, the time axis is relative to 2923 UTC, which is the beginning of the 30 min ensemble integration period preceding the first assimilation cycle.

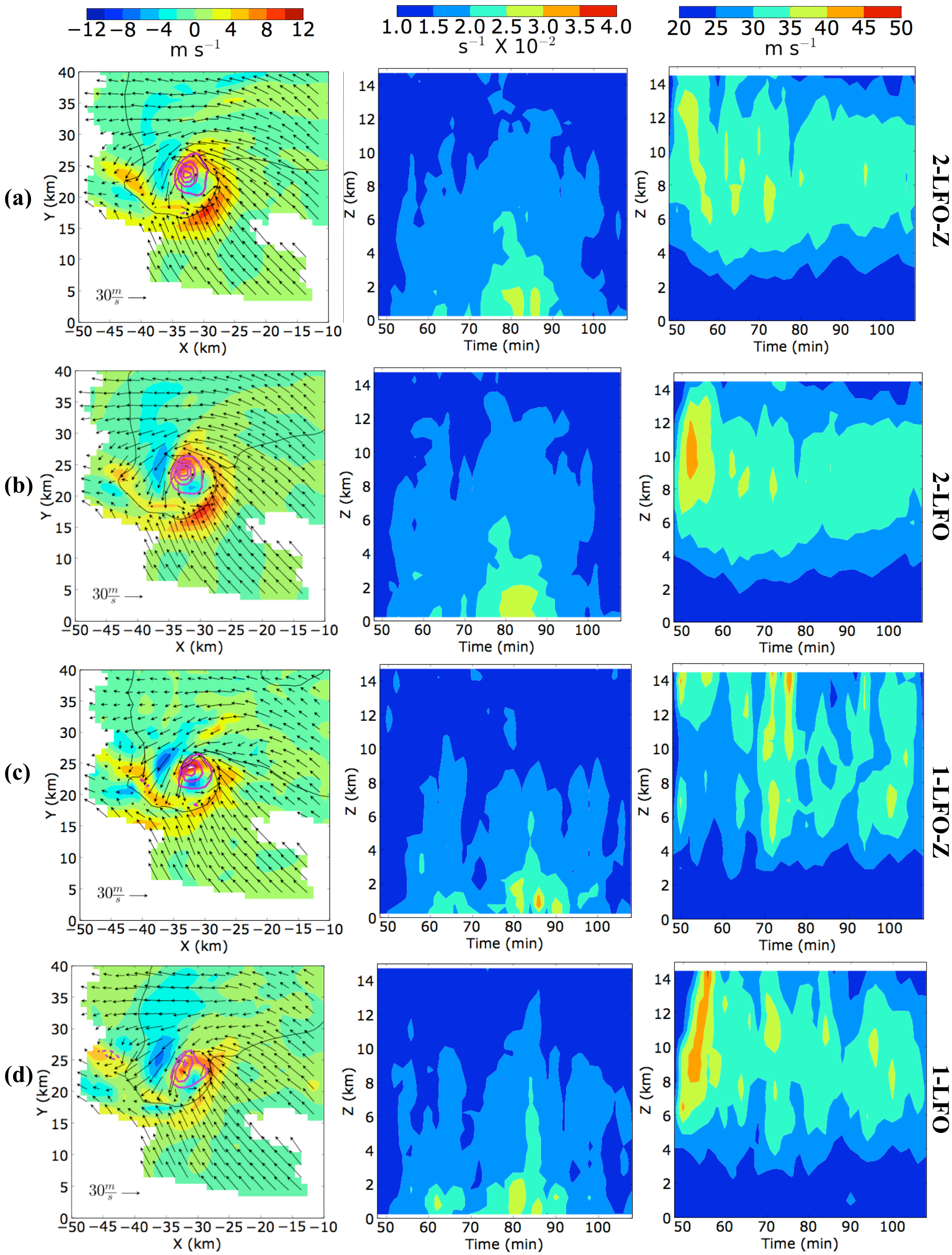

−12 −8 −4 0 4 8 12
m s−1
1.0 1.5 2.0 2.5 3.0 3.5 4.0
s−1 X 10−2
20 25 30 35 40 45 50
m s−1
(a)
(b)
(c)
(d)
Y (km)
X (km)
Z (km)
Time (min)
30 m/s
2-LFO-Z
2-LFO
1-LFO-Z
1-LFO

Figure 5. Kinematical analyses from (a) 2-LFO-Z, (b) 2-LFO, (c) 1-LFO-Z and (d) 1-LFO. Left panels: horizontal winds (arrows), w (shading), ζ (magenta contours, plotted every .01 s^{-1} beginning at .01 s^{-1}), and dBZ = 10 (black contour) at z = 500 m, 0033 UTC; middle panels: time-height plots of mean $w > 20$ m s^{-1}; right panels: time-height plots of mean $\zeta > .01$ s^{-1}. The x and y axes are relative to the location of SR1 (Fig. 1b).

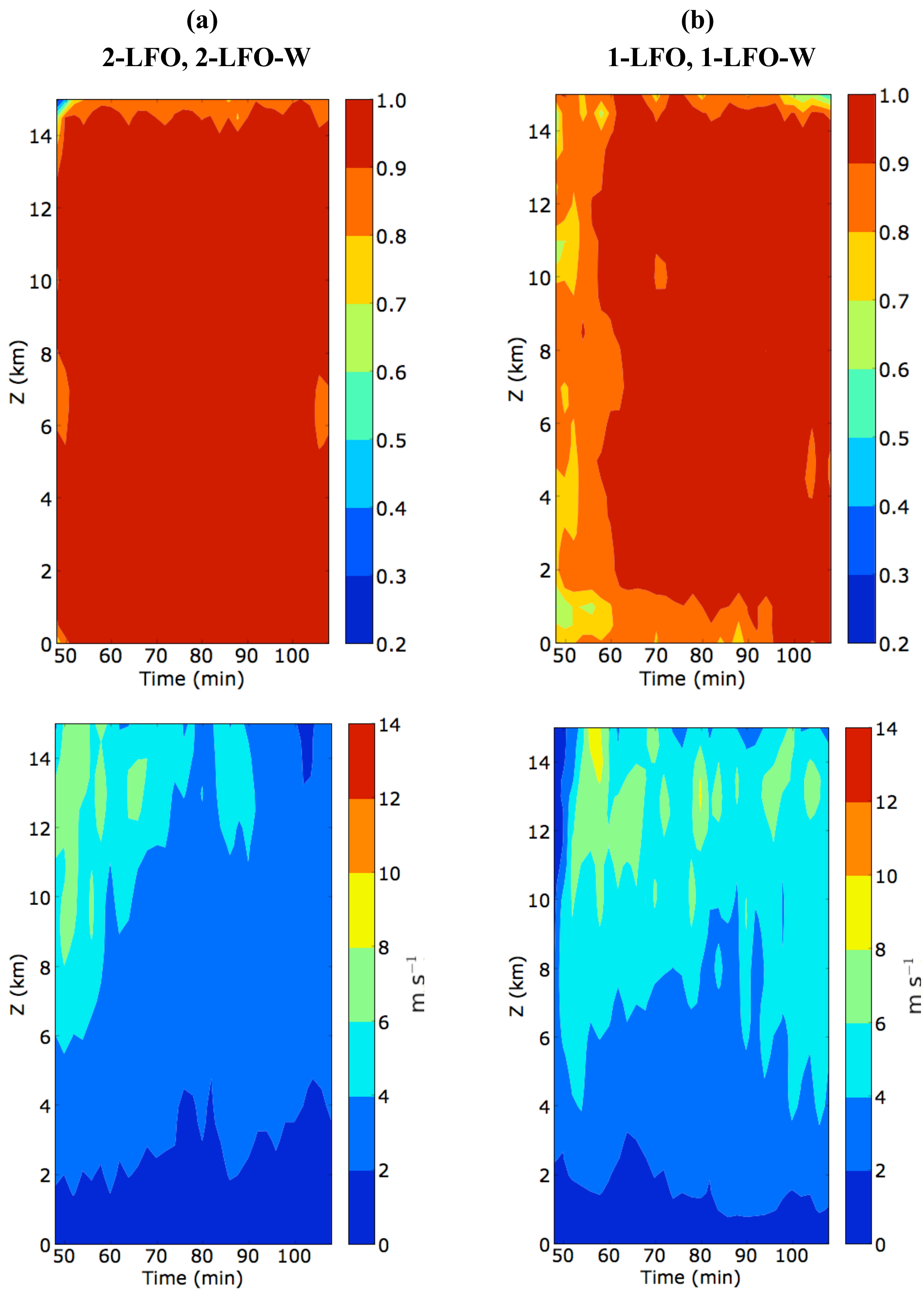

Figure 6. Time-height plots of correlation coefficient (top) and RMS difference (bottom) between *w* from (a) 2-LFO and 2-LFO-W and (b) 1-LFO and 1-LFO-W.

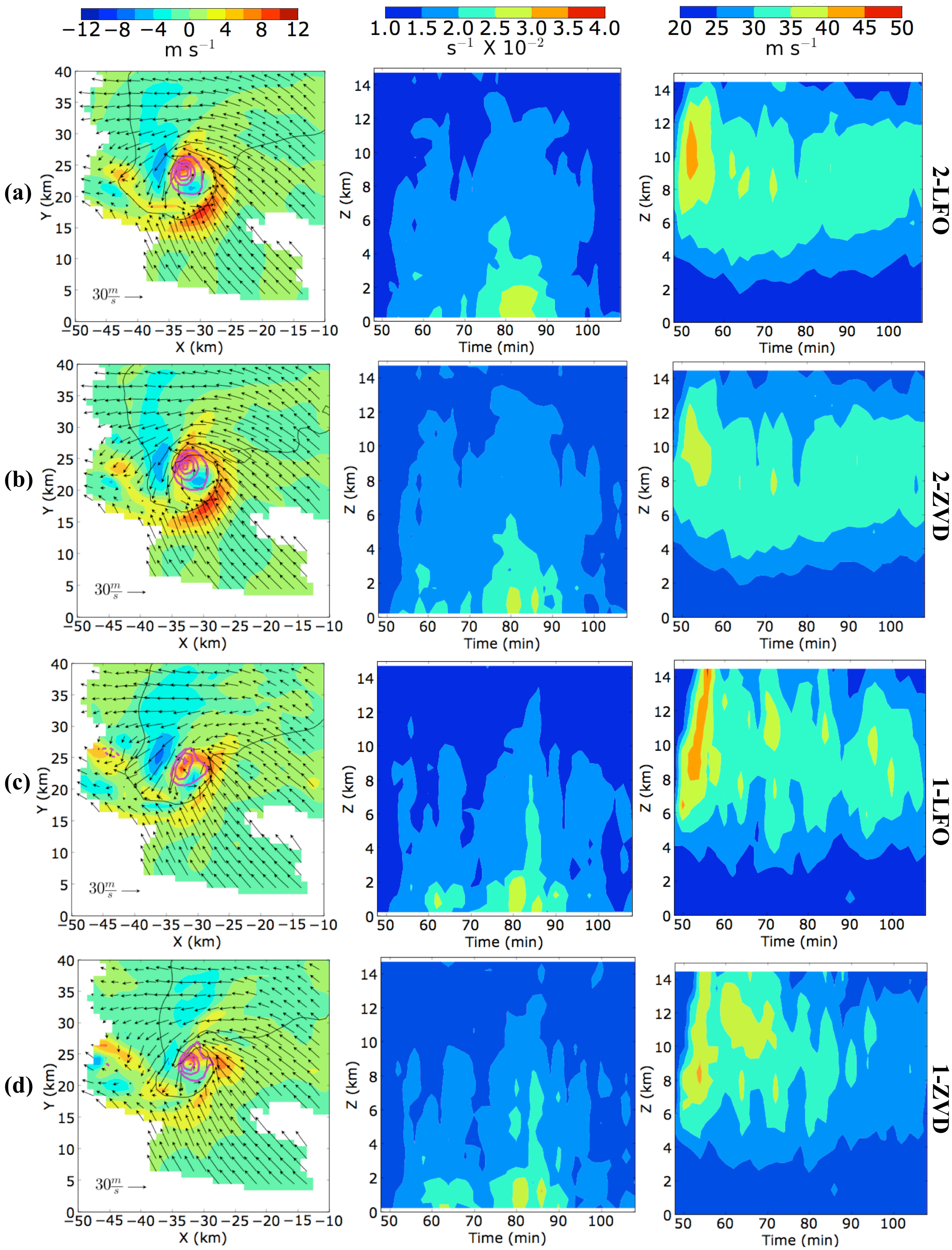

Figure 7. As in Fig. 5 but for (a) 2-LFO, (b) 2-ZVD, (c) 1-LFO and (d) 1-ZVD.

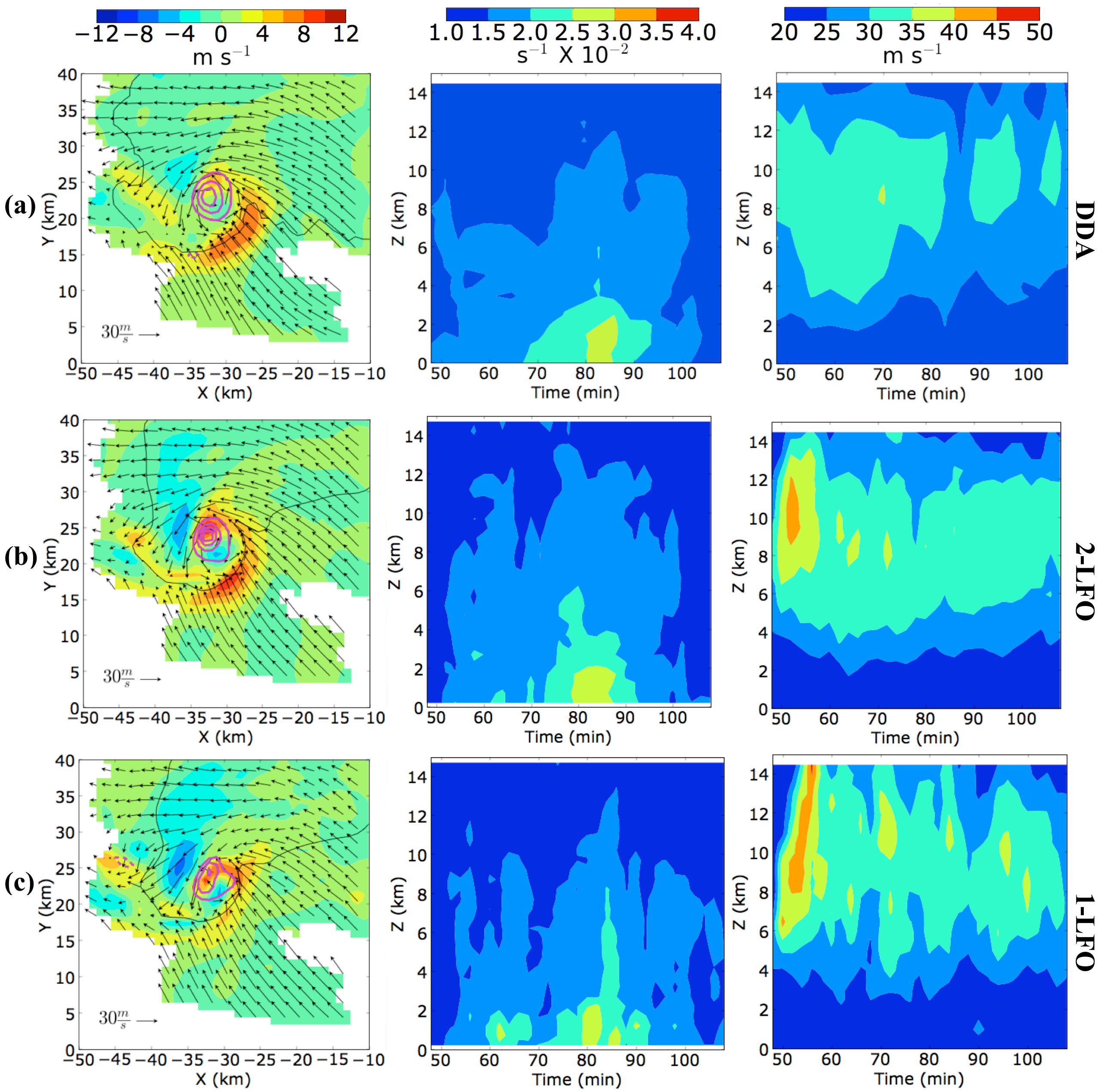

Figure 8. As in Fig. 5 but for (a) DDA, (b) 2-LFO and (c) 1-LFO.

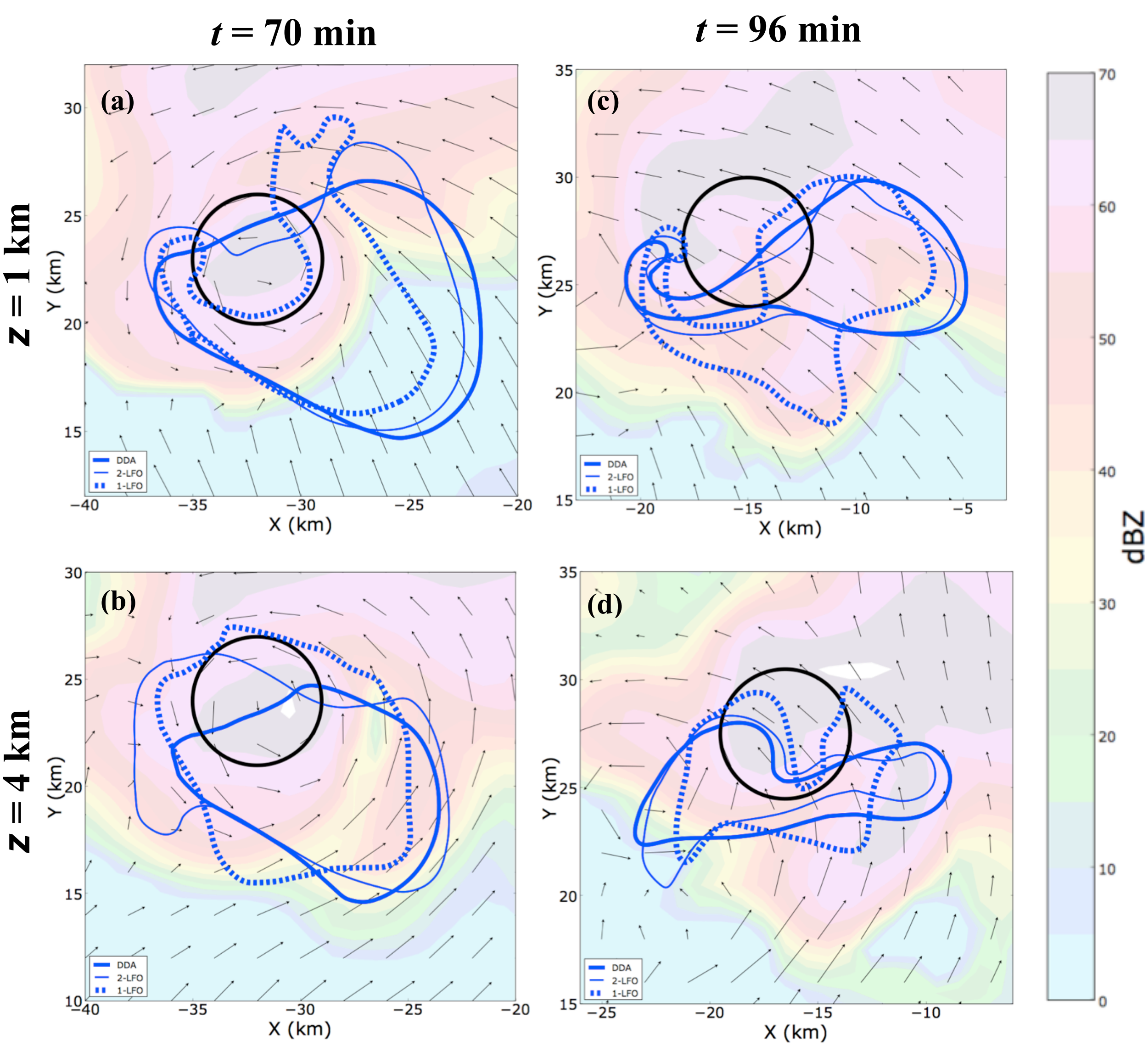

Figure 9. Horizontal projections of material circuits valid at t - 5 min. The circuits are initialized at a 3-km-radius ring (black circle) at (a) t = 70 min, z = 1 km, (b) t = 70 min, z = 4 km, (c) t = 96 min, z = 1 km and (d) t = 96 min, z = 4 km. The trajectories were computed from the (thick solid) DDA, (thin solid) 2-LFO and (dashed) 1-LFO wind analyses. The 2-LFO reflectivity (shading) and horizontal winds (arrows) valid at the time and height at which the trajectories were initialized are displayed in each panel.

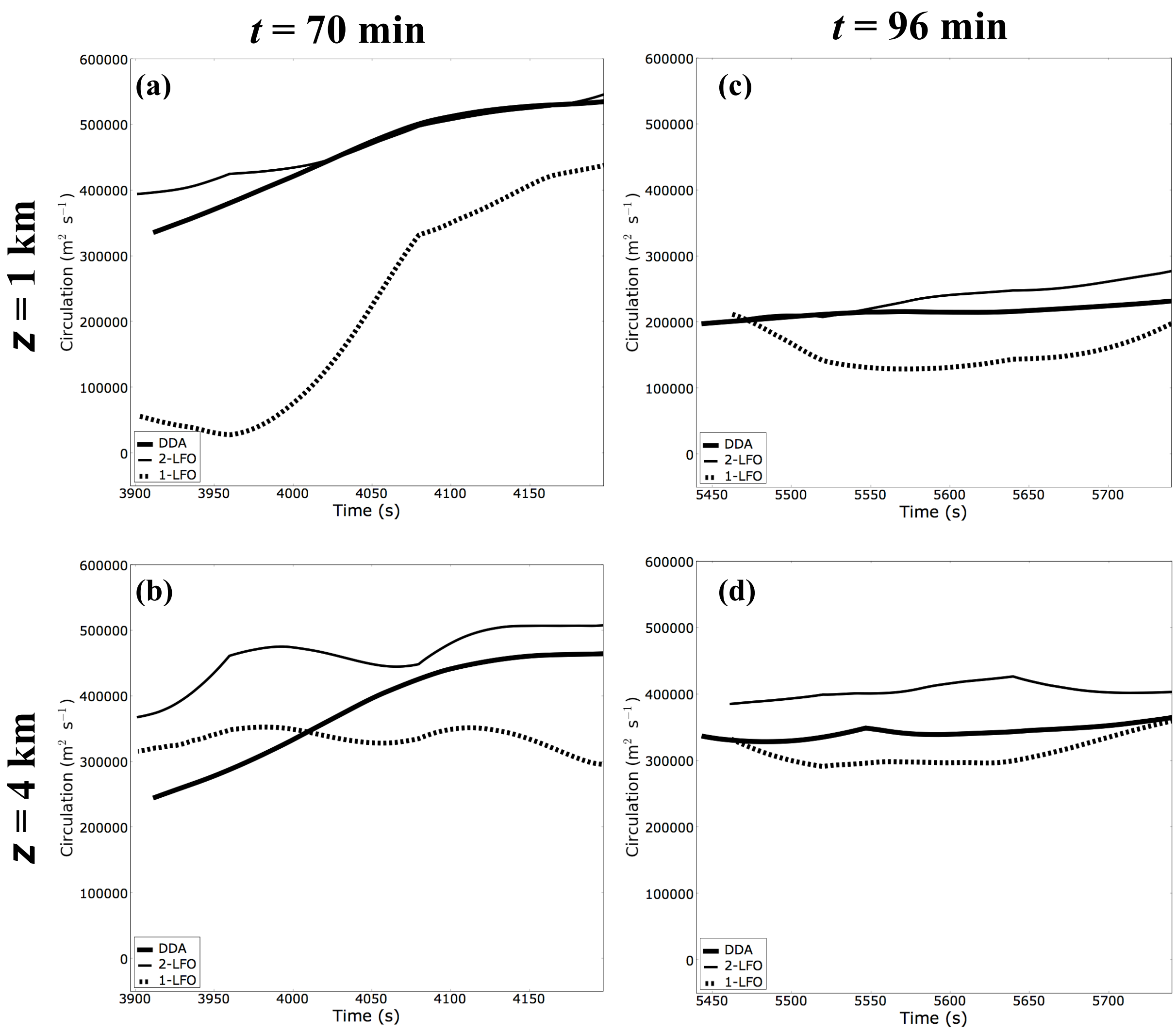

Figure 10. Time series of circulation computed around the circuits in Fig. 9 (DDA = thick, solid; 2-LFO = thin, solid; 1-LFO = dashed).